Chinese Chemical Letters 37 (2026) 111891

Contents lists available at ScienceDirect

Chinese Chemical Letters

journal homepage: www.elsevier.com/locate/cclet

Carbon dots-embedded hydrogel ratiometric fluorescent platform for portable determination of doxorubicin in clinical samples

Xin Liu[a], Haoran Zhu[a], Yi Wang[a,*], Haili Zhang[a], Yujie Li[a], Hongcheng Gao[a], Yi Han[a], Dejin Wang[a,*], Yunsheng Xia[b,*]

[a] College of Resources and Environment, Anqing Normal University, Anqing 246133, China
[b] College of Chemistry and Materials Science, Anhui Normal University, Wuhu 241000, China

ARTICLE INFO

Article history:
Received 30 April 2025
Revised 5 September 2025
Accepted 24 September 2025
Available online 24 September 2025

Keywords:
Portable platform
Carbon dots
Doxorubicin
Point-of-care monitoring
Clinical samples

ABSTRACT

Portable ratiometric fluorescent platforms have emerged as promising tools for multifarious detection, yet remain unexplored for point-of-care monitoring doxorubicin (DOX), one of clinically antineoplastic drugs. To this end, we herein develop a portable self-calibrating platform namely carbon dots (C-dots)-embedded hydrogel sensors with a smartphone-assisted high-throughput imaging device, for DOX sensing. The prepared green-emitting ($\lambda_{em} = 508$ nm) and negatively-charged C-dots (-11.40 ± 1.21 mV), which have sufficient spectral overlap with the absorption band of DOX (~500 nm), can strongly bind with positively-charged DOX molecules by electrostatic attraction effects. As a result, DOX molecules are selectively and rapid (20 s) determined with a detection limit of 10.26 nmol/L *via* Förster resonance energy transfer processes, demonstrating a remarkably chromatic shift from green to red. Further integrated with a 3D-printed smartphone-assisted device, the platform enabled high-throughput quantification, achieving recoveries of 96.40%–101.85% in human urine/serum (RSDs < 2.94%, $n = 3$). Notably, the dual linear detection ranges of the platform align with the reported clinical DOX concentrations in urine and plasma (0–4 h post-administration), validating their capability for direct quantification of DOX in clinical samples without special pre-treatment processes. By virtue of attractive analytical performances and robust feasibility, this platform bridges laboratory precision and point-of-care testing needs, offering promising potential for personalized chemotherapy and multiplexed analyte screening.

© 2025 Published by Elsevier B.V. on behalf of Chinese Chemical Society and Institute of Materia Medica, Chinese Academy of Medical Sciences.

Portable on-site detection has gained significant attention in clinical diagnosis, environmental monitoring, and food analysis due to its capacity to deliver real-time measurements and accurately reflect sample conditions [1–3]. A typical portable testing platform integrates a highly sensitive and selective sensor (*e.g.*, fluorescent, electrochemical, or colorimetric strategies) with a miniaturized signal readout device [4–7], often designed as wearable, handheld, or microfluidic modes [8–10]. Recent advancements in smartphone cameras and image processing software have further propelled the development of smartphone-integrated portable testing platforms. By exploiting diverse fluorophores, such as organic molecules, gold nanorods, and metal-organic frameworks [11–13]. These platforms have enabled the detection of multiple analytes, including biomarkers, metal ions, food additives, and pesticide residues [14–18]. Doxorubicin (DOX), one of widely used antineoplastic drugs, is clinically administered to treat various cancers, including sarcoma, breast cancer, and lung cancer, by inducing tumor cell apoptosis and DNA damage [19,20]. However, its nonspecific targeting mechanism also damages healthy cells, leading to irreversible cellular damage and systemic toxicity [21]. Additionally, interindividual variability in drug metabolism and tolerance complicates dosage regimens; studies indicate that drug overdoses exacerbate somatic toxicity and accelerate disease progression [22]. To address these challenges, developing a point-of-care DOX sensing platform is critical for enabling real-time dosage monitoring and personalized therapeutic protocols. Although conventional methods (for example, high-performance liquid chromatography and mass spectrometry) offer laboratory-grade sensitivity, they suffer from limited portability, operational simplicity, and accessibility for on-site applications [23]. Thus, advancing user-centric, accurate sensing platform remains an urgent priority.

Hydrogels, three-dimensional hydrophilic networks formed by cross-linked water-soluble polymers, have emerged as promising matrices for on-site analytical applications [24,25], overcoming limitations of liquid systems (*e.g.*, portability issues) and solid materials (*e.g.*, restricted molecular diffusion) [26]. By virtue of their

* Corresponding authors.
E-mail addresses: wangyi@aqnu.edu.cn (Y. Wang), wangdj@aqnu.edu.cn (D. Wang), xiayuns@mail.ahnu.edu.cn (Y. Xia).

https://doi.org/10.1016/j.cclet.2025.111891
1001-8417/© 2025 Published by Elsevier B.V. on behalf of Chinese Chemical Society and Institute of Materia Medica, Chinese Academy of Medical Sciences.

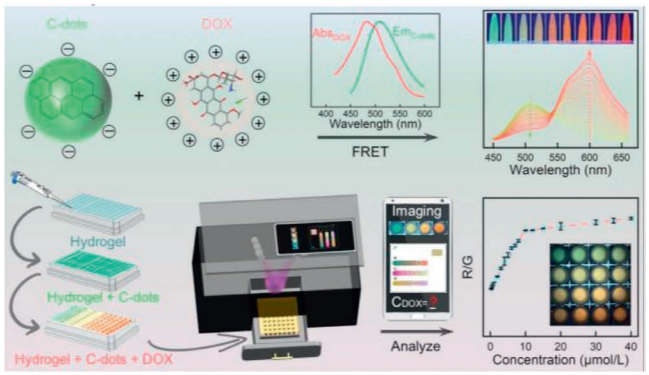


Fig. 1. Schematic diagram of ratiometric fluorescent sensing mechanism of the C-dots embedded hydrogel sensors and multi-channel determining procedure of the portable platforms.

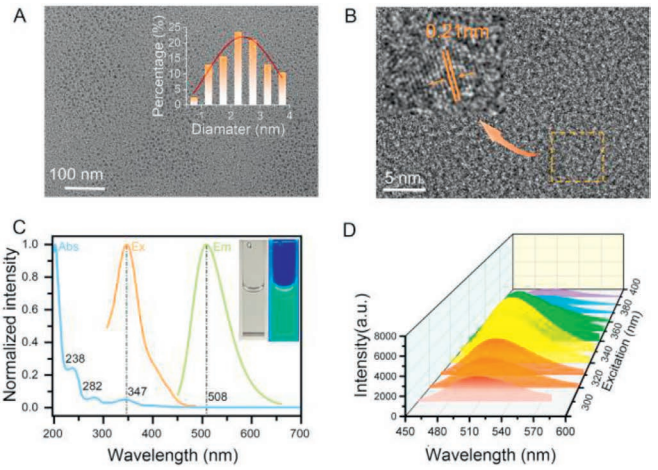


Fig. 2. Morphological characterizations and optical properties of the C-dots. (A) TEM image (inset: size distribution, $n = 200$). (B) HRTEM image. (C) UV-vis absorption (blue), fluorescence excitation (orange), and emission (green) spectra (inset: C-dots solutions under ambient light and 365 nm UV excitation). (D) Emission spectra with different excitation wavelengths.

advantages of chemical inertness, optical stability, and tunable fluorescence, carbon dots (C-dots) have been employed for integrating with hydrogels to detect various ions and molecules [27–29]. However, some existing fluorescent platforms depend on oversimplified "turn-on/off" responses lacking intrinsic self-calibration or anti-interference mechanisms, which compromises sensitivity, accuracy, and practicability in complex matrices. Therefore, engineering ratiometric C-dots embedded hydrogel sensors with self-calibration capacity is an essential step toward reliably quantitative measurement under practical conditions [30,31]. Meanwhile, emerging smartphone-integrated fluorescent platforms based on digital image colorimetry have been utilized for analyte detection and quantification based on solution-phase, hydrogel, or paper-based modes [32–34]. Nevertheless, these platforms are mostly confined to single-sample analysis per detection chamber, necessitating repetitive measurements to derive mean values and standard deviations. To address this issue, the development of multi-channel detection modules capable of simultaneous multi-sample imaging would not only enhance throughput but also improve statistical reliability by enabling systematic evaluation of experimental variability.

Herein, a portable smartphone-based device integrated with a ratiometric fluorescent C-dots embedded hydrogel sensor is developed for on-site fluorescent monitoring of DOX. Specifically, the green-emitting C-dots (peaking at 508 nm) are engineered to spectrally overlap with the distinctive absorption band of DOX (~500 nm). Upon DOX addition, the C-dots embedded hydrogel sensors exhibited a highly selective and sensitive (10.26 nmol/L) responding to DOX, *via* electrostatically driven proximity and Förster resonance energy transfer (FRET) mechanism, leading to a visible chromatic shift from green to red with International Commission on Illumination (CIE) coordinates changing from (0.24, 0.52) to (0.52, 0.45). For point-of-care testing, the proposed sensors are injected into a 96-well plate, which is then loaded into the drawer-style sample chamber of the portable device (Fig. 1). Due to the simultaneous determination of multiple samples in the plate, the tailored platform enables high-throughput DOX quantification with high reliability. As a result, real-sample validation of the platform yields recoveries of 96.40 %–101.85 % in human urine/serum (RSDs < 2.94 %, $n = 3$) and 98.90 %–114.65 % in environmental water (RSDs < 7.32 %, $n = 3$). This strategy not only establishes a highly competent platform for clinical DOX monitoring but demonstrates promising potential for expanding on-site rapid detection technologies to multiplexed analyte screening.

The preparation and purification of the C-dots are slightly modified from our previous reports [35,36]. Given the distinctive absorption band of DOX (~500 nm) (Fig. S1 in Supporting information), the C-dots with an emission peak near 500 nm are rationally engineered to maximize spectral overlap, thereby establishing an ideal platform for DOX sensing *via* FRET mechanisms (Fig. 1). The C-dots are fabricated *via* one-pot solvothermal method using m-aminophenol as the sole precursor, where optimal reaction parameters (160 °C, 3 h) are identified through systematic screening (Figs. S2 and S3 in Supporting information). Crude C-dots are subjected to prefiltration and silica gel column chromatography to eliminate unreacted precursors and byproducts, and highly purified C-dots are obtained (Fig. S4 in Supporting information).

Morphological and structural characteristics of the purified C-dots are investigated by transmission electron microscopy (TEM) and high-resolution TEM (HRTEM). As shown in Fig. 2A, the TEM image reveals high monodispersity of the C-dots, and the particle diameters range from 0.75 nm to 3.75 nm with an average size of 2.42 nm ($n = 200$). Moreover, the HRTEM image (Fig. 2B) demonstrates well-resolved lattice fringes with a d-spacing of 0.21 nm, matching the (100) crystallographic plane of graphitic carbon, which confirms the graphitic structure of the C-dots [37,38].

The optical properties of the C-dots are then systematically investigated. The UV-vis absorption spectrum (Fig. 2C, blue line) exhibits three distinct peaks at 238 nm (π-π^* transition of C=C/C–C bonds), 282 nm (n-π^* transition of C=O/C–N groups), and 347 nm (attributed to surface state transitions), confirming the multifunctional electronic structures of the C-dots [39,40]. Notably, the absence of absorption in the visible region renders the C-dots solution optically transparent under ambient light (Fig. 2C, left inset), minimizing background interference in following colorimetric detection. Excitation-independent emission behavior is evidenced by the invariant emission peak at 508 nm across excitation wavelengths (300–400 nm) (Fig. 2D and Fig. S5 in Supporting information), precisely matching the designed FRET mechanism for sensing DOX with a characteristic absorption band near 500 nm. By virtue of a highly absolute fluorescence quantum yield of 38.23 %, the C-dots solution is endowed with brightly green emission under UV light (Fig. 2C, right inset). Furthermore, the excitation spectrum ($\lambda_{em} = 508$ nm, Fig. 2C, orange line) displays a peak at 347 nm, aligning with the third absorption band and optimal excitation wavelength, thereby validating the suggested energy transfer mechanism. Time-resolved fluorescence decay analysis (Fig. S6 in Supporting information) revealed a single-exponential lifetime of 5.12 ns ($\chi^2 = 1.23$), suggesting a single radiative recombination pathway of the C-dots. Due to the protonation/deprotonation effects, the C-dots exhibit pH-dependent fluorescent intensities (Fig. S7 in Supporting infor-

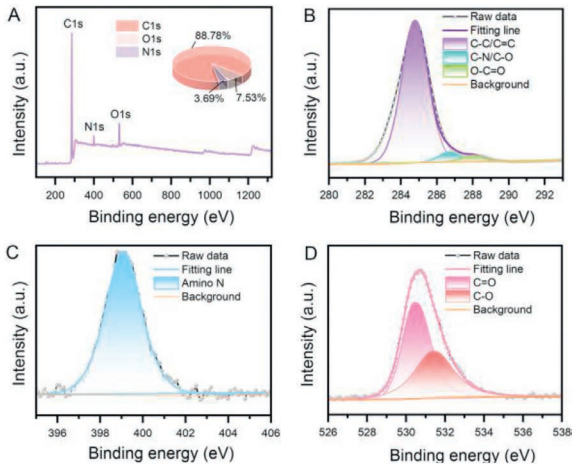


Fig. 3. (A) Survey XPS spectra of the C-dots. High-resolution XPS spectra of C 1s (B), N 1s (C), and O 1s (D), respectively.

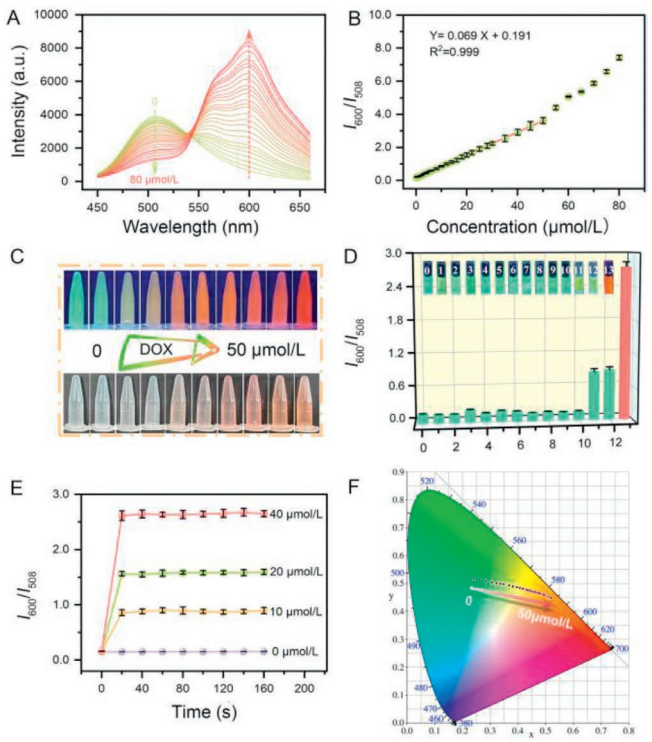


Fig. 4. Analytical performances of the C-dots sensing DOX. (A) Fluorescence spectra of the C-dots with incremental DOX concentrations (0–80 μmol/L). (B) Linear relationship between I_{600}/I_{508} and DOX concentrations. (C) Concentration-dependent chromatic transition images of C-dots solution under 365 nm (upper) and ambient light (lower). (D) Selectivity of the sensors against other typical antibiotics (0, blank; 1, tetracycline; 2, erythromycin; 3, chloramphenicol; 4, oxytetracycline; 5, aureomycin hydrochloride, 6, gentamycin; 7, penicillin potassium; 8, cefazolin; 9, ciprofloxacin; 10, doxycycline; 11, epirubicin; 12, idarubicin; 13, DOX; insets are the corresponding fluorescent images under 365 nm light). (E) Reaction kinetics curves for different concentrations of DOX. (F) CIE coordinates shift for incremental DOX concentrations. Data are presented as mean ± standard deviation (SD) ($n = 3$).

mation). Considering the pH value of physiological environment, 7.40 is chosen as the condition for the subsequent measurements. Additionally, the C-dots have excellent batch reproducibility of their fluorescent emission (Fig. S8 in Supporting information) and photostability under long-term ultraviolet irradiation, high salinity environment, and long-term storage (Figs. S9–S11 in Supporting information). These results affirm the C-dots as a robust, design-compliant fluorescent probe tailored for DOX sensing.

Chemical compositions and surface states of the C-dots are analyzed *via* X-ray photoelectron spectroscopy (XPS) and Fourier transform infrared spectroscopy (FTIR). As shown in the XPS survey spectrum (Fig. 3A), the C-dots consist of carbon (284.80 eV, 88.78 at%), nitrogen (399.08 eV, 3.69 at%), and oxygen (530.48 eV, 7.53 at%). High-resolution C 1s spectrum (Fig. 3B) can be deconvoluted into three components at 284.80 eV (C–C/C=C), 286.68 eV (C–N/C–O), and 288.08 eV (O–C=O), confirming the coexistence of aromatic and oxygen/nitrogen-containing functional groups [41]. N 1s spectrum (Fig. 3C) exhibits a single peak at 399.08 eV assigned to amino ($-NH_2$) groups, indicating successful retention of precursor-derived nitrogen moieties during carbonization. O 1s analysis (Fig. 3D) resolves two peaks at 530.48 eV (C=O) and 531.38 eV (C–O), consistent with carbonyl and hydroxyl/ether groups. FTIR analysis (Fig. S12 in Supporting information) reveals characteristic absorption bands at 3290 cm^{-1} (N–H stretching), 2930 cm^{-1} (C–H stretching), 1630 cm^{-1} (C=C aromatic stretching), and 1000–1250 cm^{-1} (C–N stretching/bending modes), respectively [42,43]. These results validate the hybrid carbon structure with abundant oxygen/nitrogen surface states, which are critical for enhancing the hydrophilicity and fluorescence properties of the C-dots.

To validate the sensing platform, the C-dots solution is titrated with incremental DOX concentrations (0–80 μmol/L). As depicted in Fig. 4A, the emission intensity at 508 nm decreases progressively, while a new emission band emerges at 600 nm, leading to a ratiometric fluorescence intensities response (I_{600}/I_{508}) linearly correlated with DOX concentrations ($Y = 0.069\ X + 0.191$, $R^2 = 0.999$, 0.20–50 μmol/L) (Fig. 4B). The calculated limit of detection (LOD) of 10.26 nmol/L surpasses most reported methods, including fluorescence, electrochemical, high-performance liquid chromatography (Tables S1 and S2 in Supporting information), and concentration-based assay (Fig. S14 in Supporting information), exhibiting a highly sensitive detection. In addition, a concentration-dependent chromatic transition from green to red is also observed under UV light (Fig. 4C, upper panel), corresponding to a CIE coordinate shift from (0.24, 0.52) to (0.52, 0.45) (Fig. 4F). Remarkably, the colorimetric change is discernible to the naked eye under ambient light (Fig. 4C, lower panel), prompting further investigation *via* absorption spectroscopy. UV-vis absorbance of the C-dots solution also increases proportionally with DOX concentration (Fig. S15 in Supporting information), with a distinct absorption band at 470–502 nm serving as the detection window. Normalized absorbance ratios (A/A_0) also demonstrate a linear relationship with DOX levels ($Y = 8.477\ X - 4.165$, $R^2 = 0.999$), yielding a colorimetric LOD of 51.20 nmol/L.

The selectivity of the sensors is evaluated against typical interferences, including antibiotics, amino acids, co-medications, anions, and metal ions (100 μmol/L). Except for epirubicin and idarubicin, interference groups exhibited I_{600}/I_{508} values comparable to that of the control group (Fig. 4D and Fig. S16 in Supporting information) [44]. Due to the same absorption peaks near 500 nm, epirubicin and idarubicin can cause fluorescence quenching of the C-dots. However, in view of their similar pharmacological effects and higher toxicity risk, anthracycline drugs are generally not used in combination in actual treatment [45,46]. In addition, selective studies on co-medications (cytarabine, glucose) indicate that they have negligible influence in the sensing of DOX [47]. Accordingly, the C-dots based sensors have a competent specificity for sensing DOX in actual samples.

Reaction kinetics measurements (Fig. 4E) discover that I_{600}/I_{508} values reach equilibrium within 20 s after introducing DOX (10, 20, 40 μmol/L), indicating that the reactions between C-dots and DOX have superfast speed. This rapid response enables the capacity of on-site analysis of the sensors, a critical advantage for point-of-care monitoring.

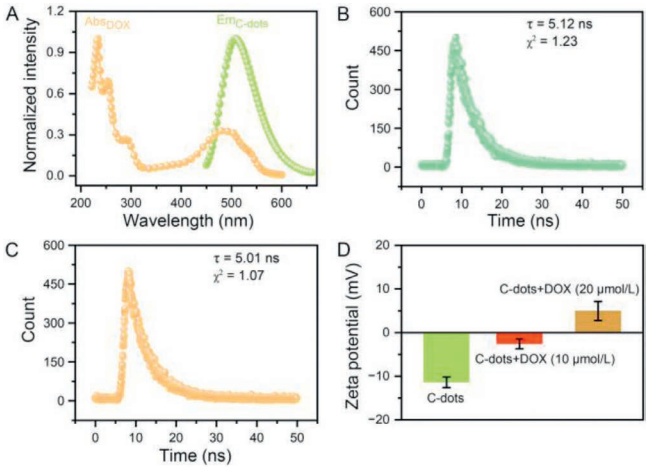


Fig. 5. (A) UV-vis absorption spectrum of DOX (orange), fluorescence emission spectrum of the C-dots (green). Time-resolved fluorescence decay curves of the C-dots (B) and C-dots+DOX (C) (λ_{em} = 508 nm). (D) Zeta potentials of the C-dots and C-dots+DOX (10, 20 μmol/L). Data are presented as mean ± SD (n = 3).

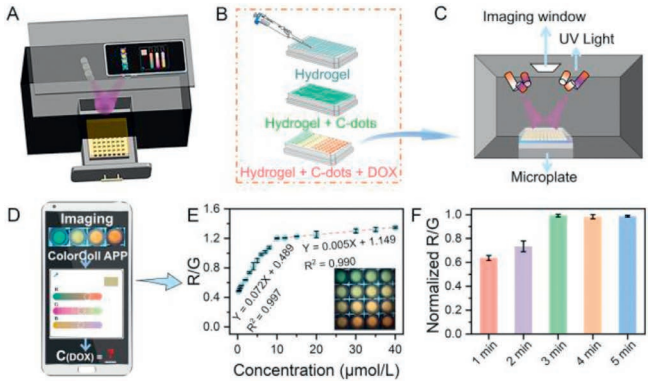


Fig. 6. Smartphone-integrated sensing platform for determination of DOX. (A) Schematic diagram of smartphone-integrated imaging device. (B) Addition of DOX into C-dots embedded hydrogel sensors in 96-well plate. (C) Fluorescent imaging of 96-well plate. (D) Quantification of R/G signals by ColorColl APP. (E) Linear relationship between R/G values and DOX concentrations measured through the proposed platform (hydrogel: 0.50 %). (F) Time-resolved fluorescence kinetics of C-dots responding to DOX within hydrogel. Data are presented as mean ± SD (n = 3).

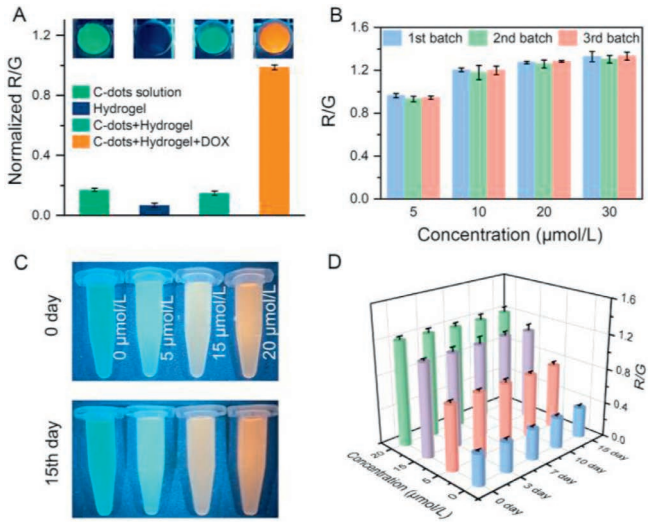


Fig. 7. (A) Fluorescent images of the C-dots solution, hydrogel, C-dots+hydrogel, C-dots+hydrogel+DOX, and the corresponding normalized R/G ratios. (B) The R/G ratios for different DOX concentrations from different hydrogel-based sensor batches. Fluorescent images of C-dots embedded hydrogel stored at room temperature under ambient light for 15 days (C) and the corresponding R/G ratios with incremental days (D). Data are presented as mean ± SD (n = 3).

The proposed FRET mechanism is verified by spectroscopic and surface charge analyses. As illustrated in Fig. 5A, the absorption spectrum of DOX exhibits strong spectral overlap with the emission band of C-dots, fulfilling the critical Förster distance requirement for efficient energy transfer. Time-resolved fluorescence decay measurements (Figs. 5B and C) of the C-dots solution reveal comparable lifetimes for the absence (5.12 ns) and presence of DOX (5.01 ns), ruling out electron transfer processes and confirming FRET dominance [48,49]. Zeta potential measurements demonstrate that the C-dots are negatively charged (−11.40 ± 1.21 mV). As positively charged DOX molecules with 10, 20 μmol/L are respectively introduced into the C-dots solution, [50,51], the zeta potential values the (C-dots+DOX) mixtures change to −2.56 mV and 4.95 mV (Fig. 5D), verifying electrostatic attraction-driven proximity between the probes and targets. This close association facilitates FRET-mediated ratiometric sensing, enabling rapid (<20 s) and highly selective DOX quantification.

To enable point-of-care DOX monitoring, the C-dots are embedded into hydrogel to enhance portability and stability, which is further integrated with a 3D-printed imaging device (Fig. S17 in Supporting information) comprising black outer shell, drawer-style sample chamber (96-well plate compatible), UV light modules, and imaging window (Fig. 6A). Hydrogel and C-dots are successively dispensed into 96-well plates (Fig. 6B), enabling simultaneous determination of multiple samples and high-throughput analysis. Upon addition of DOX, fluorescent images of 96-well samples are captured through the imaging window by smartphone (Fig. 6C), which are subsequently processed *via* a ColorColl APP to quantify ratiometric signals (R/G) (Fig. 6D). Dual linear calibration curves are established for DOX sensing as $Y = 0.072X + 0.489$ ($R^2 = 0.997$, 0.30–10 μmol/L) and $Y = 0.005X + 1.149$ ($R^2 = 0.990$, 10–40 μmol/L), achieving an LOD of 42.41 nmol/L (Fig. 6E). Studies reveal that the DOX concentrations in the clinical urine and plasma are 16.30–30.80 μmol/L and 0.17–0.32 μmol/L at 0–4 h post-administration [52]. Remarkably, the concentration ranges align with the dual linear ranges of the established calibration curves, respectively, indicating the platform's capability for direct quantification in patient samples without special pre-treatment [53]. In addition to iPhone 13 (Fig. 6E), cross-device validation using Vivo and Huawei smartphones demonstrates consistent linear relationship despite minor slope variations (Fig. S18 in Supporting information), indicating that differences in smartphone brands have no influence on the detection results. Meanwhile, comprehensive experiments with different proportions of hydrogel verify that the proportions also do not affect the detection results (Fig. S19 in Supporting information). Time-resolved fluorescence kinetics studies (Fig. 6F) reveal that the interactions of the C-dots and DOX within the hydrogel can reach equilibrium within 3 min, fulfilling real-time analysis requirements for point-of-care testing.

The imaging feasibility and optical stability of the proposed platform are then systematically evaluated. As shown in Fig. 7A, the non-fluorescent hydrogel (control) exhibits negligible background signals, ensuring high signal-to-noise ratios for subsequent analyses. Upon sequential incorporation of the C-dots and DOX, the hydrogel emits spatially uniform green and orange fluorescence, confirming homogeneous C-dots distribution and reliable colorimetric readout accuracy (Fig. 7A). In addition, the C-dots embedded hydrogel sensors from different batches demonstrate favorable reproducibility (Fig. 7B). Long-term storage assessments further reveal that the sensors have consistent fluorescence intensities and R/G ratios over 15 days (Figs. 7C and D). These results validate ex-

Table 1
Sensing DOX in human urine and serum by spiked recovery experiments ($n = 3$).

Samples	Images	Spiked (μmol/L)	Found (μmol/L)	Recovery (%)	RSD (%, $n = 3$)
Urine		3.00	3.02	100.67	1.31
		10.00	9.87	98.70	2.94
		20.00	20.03	100.15	1.71
Serum		3.00	2.98	99.33	1.83
		10.00	9.64	96.40	1.59
		20.00	20.37	101.85	2.64

ceptional chemical and optical stability of the sensors, providing the prerequisite for the subsequent practical utility.

To validate the clinical applicability of the proposed platform for DOX sensing, spiked recovery experiments in actual samples are adopted. Calibration operations in human serum and urine are first conducted, which indicates that the platform has good anti-interference capability in complex physiological matrix (Fig. S20 in Supporting information). Then, urine and serum samples (from healthy volunteers) are spiked with DOX (3, 10, 20 μmol/L) and analyzed, yielding recoveries of 96.40 %–101.85 % with RSD < 2.94 % ($n = 3$) (Table 1). In addition, environmental monitoring feasibility is also assessed by analyzing DOX-spiked environmental water samples from four sources: ultrapure water, tap water, lake water (Shuanglong Lake, Anqing Normal University), and river water (Yangtze River). The resulting recoveries ranged from 98.90 % to 114.65 % with RSD < 7.32 % (Table S3 in Supporting information), demonstrating reliable performance in environmentally relevant matrices despite inherent complexity. It should be emphasized that since multiple samples are imaged simultaneously by the proposed platform, the mean and SD of actual samples can be calculated for one measurement, avoiding multiple repeated and tedious operations. This platform addresses dual challenges in point-of-care monitoring and environmental risk assessment, offering a robust solution for bridging laboratory-grade precision with field-deployable operation.

This study introduces a fluorescence ratiometric platform for on-site DOX monitoring by integrating C-dots embedded hydrogel sensors with 3D-printed portable devices. Ratiometric fluorescent sensing, electrostatically driven proximity and FRET mechanisms enable a highly sensitive/selective and rapid response of C-dots to DOX; The linear detection ranges align with the reported clinical DOX concentrations, validating the platform's capability for direct quantification in patient samples without special pre-treatment; The 3D-printed high-throughput module not only eliminates repetitive measurements but also improves statistical reliability. Therefore, the platform not only provides an innovation in point-of-care monitoring and on-site environmental assessment, but also offers a promising potential for advancing personalized cancer therapeutics and environmental remediation strategies.

Declaration of competing interest

The authors declare that they have no known competing financial interests or personal relationships that could have appeared to influence the work reported in this paper.

CRediT authorship contribution statement

Xin Liu: Writing – original draft, Methodology, Investigation, Formal analysis. **Haoran Zhu:** Investigation, Data curation. **Yi Wang:** Writing – review & editing, Supervision, Resources, Funding acquisition. **Haili Zhang:** Visualization, Data curation. **Yujie Li:** Formal analysis. **Hongcheng Gao:** Investigation. **Yi Han:** Formal analysis. **Dejin Wang:** Supervision, Funding acquisition. **Yunsheng Xia:** Writing – review & editing, Funding acquisition.

Acknowledgments

This work was financially supported by the National Natural Science Foundation of China (No. 22274001), the Key Project of Natural Science Research of the Education Department of Anhui Province (No. 2022AH051032), and the Excellent Research and Innovation Team of Universities in Anhui Province (No. 2024AH010016).

Supplementary materials

Supplementary material associated with this article can be found, in the online version, at doi:10.1016/j.cclet.2025.111891.

References

[1] G. Xun, S.T. Lane, V.A. Petrov, B.E. Pepa, H. Zhao, Nat. Commun. 12 (2021) 2905.
[2] J.K. Jung, K.K. Alam, M.S. Verosloff, et al., Nat. Biotechnol. 38 (2020) 1451–1459.
[3] Y. Shen, Y. Wei, C. Zhu, J. Cao, D.M. Han, Coord. Chem. Rev. 458 (2022) 214442.
[4] J. Wu, W. Liu, J. Ge, H. Zhang, P. Wang, Chem. Soc. Rev. 40 (2011) 3483–3495.
[5] Z. Cao, C. Li, Y. Shu, et al., J. Am. Chem. Soc. 145 (2023) 26425–26434.
[6] L. Guo, T. Wang, Z. Wu, et al., Adv. Mater. 32 (2020) 2004805.
[7] X. Xu, A. Liu, D. Pang, Chem. Res. Chin. Univ. 40 (2024) 162–172.
[8] C. Ye, M. Wang, J. Min, et al., Nat. Nanotechnol. 19 (2024) 330–337.
[9] M. Sun, M. Liang, R. Kong, et al., Anal. Chem. 96 (2024) 17907–17913.
[10] S. Banerjee, P. Das, Sens. Actuators B: Chem. 401 (2024) 135002.
[11] Y. Liu, Y. Li, S. Koo, et al., Chem. Rev. 122 (2022) 209–268.
[12] Y. Xia, L. Song, C. Zhu, Anal. Chem. 83 (2011) 1401–1407.
[13] S. Wu, H. Min, W. Shi, P. Cheng, Adv. Mater. 32 (2020) 1805871.
[14] Q. Zhou, X. Wang, K. Tang, et al., Talanta 278 (2024) 126402.
[15] Y. Shi, W. Li, X. Feng, et al., Food Chem. 344 (2021) 128694.
[16] L. Guo, D.M. Zhao, S. Chen, Y.L. Yu, J.H. Wang, Anal. Chem. 94 (2022) 14004–14011.
[17] R. Umapathi, S.M. Ghoreishian, S. Sonwal, et al., Coord. Chem. Rev. 453 (2022) 214305.
[18] L. Tian, C. Cheng, Z. Zhao, W. Liu, L. Qi, Chem. Res. Chin. Univ. 39 (2023) 1092–1099.
[19] S. Sritharan, N. Sivalingam, Life Sci. 278 (2021) 119527.
[20] F. Yang, S.S. Teves, C.J. Kemp, S. Henikoff, Biochim. Biophys. Acta Rev. Cancer 1845 (2014) 84–89.
[21] H. Stower, Nat. Med. 26 (2020) 163.
[22] W.D. Tap, R.L. Jones, B.A. Van Tine, et al., Lancet 388 (2016) 488–497.
[23] J.B. Katzenmeyer, C.V. Eddy, E.A. Arriaga, Anal. Chem. 82 (2010) 8113–8120.
[24] Y. Wang, T. Lv, K. Yin, et al., Small 19 (2023) 2207048.
[25] Y. Hu, C.H. Lu, W. Guo, et al., Adv. Funct. Mater. 25 (2015) 6867–6874.
[26] Z.H. Yang, J. Yin, L. Xin, et al., Chin. Chem. Lett. 35 (2024) 109558.
[27] Y. Hu, O. Seivert, Y. Tang, H.E. Karahan, A. Bianco, Angew. Chem. Int. Ed. 63 (2024) 202412341.
[28] J. Zhang, J. Jin, J. Wan, et al., Chem. Eng. J. 408 (2021) 127351.
[29] H. Liu, X. Sun, Y. Dai, X. Zhang, F. Xia, Chem. Res. Chin. Univ. 40 (2024) 326–332.
[30] S. Xu, L. Li, D. Lin, et al., Chin. Chem. Lett. 34 (2023) 107997.
[31] M. Xie, J. Chen, Y. Wang, et al., Chin. Chem. Lett. 35 (2024) 108575.
[32] Y. Fan, J. Li, Y. Guo, L. Xie, G. Zhang, Measurement 171 (2021) 108829.
[33] X. Mao, M. Shi, C. Chen, et al., Biosens. Bioelectron. 247 (2024) 115919.
[34] Q. Zhang, Z. Zhang, S. Xu, et al., J. Hazard. Mater. 436 (2022) 129320.
[35] Y. Wang, G. Guo, J. Gao, et al., Chem. Mater. 32 (2020) 8146–8157.
[36] Y. Wang, Z. Li, G. Guo, Y. Xia, Anal. Chem. 95 (2023) 2765–2773.
[37] D.W. Boukhvalov, V.Y. Osipov, D. Murzalinov, A. Serikkanov, H. Bi, Carbon 225 (2024) 119101.
[38] S. Li, Q. Zhou, Z. Li, M. Liu, Y. Li, Chin. Chem. Lett. 35 (2024) 108693.
[39] S. Lu, G. Xiao, L. Sui, et al., Angew. Chem. Int. Ed. 56 (2017) 6187–6191.
[40] M. Liang, G. Song, Y. Wan, et al., Chin. Chem. Lett. 35 (2024) 108573.
[41] G. Guo, Y. Xia, Anal. Chem. 96 (2024) 5095–5105.
[42] M. Liu, X. Hao, S. Dai, et al., Chem. Res. Chinese Univ. 39 (2023) 234–239.
[43] M. Zhao, M. Lin, G. Guo, Y. Xia, Anal. Chem. 96 (2024) 20169–20178.
[44] C. Kreukler, K.U. Köhrmann, P. Alken, M.J. Siegsmund, A. Steidler, Eur. Urol. 31 (2017) 365–370.
[45] R.J. Cersosimo, W.K. Hong, J. Clin. Oncol. 4 (1986) 425–439.
[46] M.A. Le Bot, J.M. Bégué, D. Kernaleguen, et al., Biochem. Pharmacol. 37 (1988) 3877–3887.
[47] W.R. Bezwoda, R.D. Dansey, Leuk. Lymphoma 1 (1990) 221–225.

[48] H. Yao, Y. Zhang, F. Xiao, Z. Xia, J. Rao, Angew. Chem. Int. Ed. 46 (2007) 4346–4349.
[49] W.R. Algar, N. Hildebrandt, S.S. Vogel, I.L. Medintz, Nat. Methods 16 (2019) 815–829.
[50] M. Szota, B. Jachimska, Pharmaceutics 15 (2023) 875.
[51] B. Jachimska, M. Goncerz, P. Wolski, et al., Mol. Pharm. 21 (2024) 5892–5904.
[52] O. Maliszewska, A. Plenis, I. Olędzka, et al., J. Pharm. Biomed. Anal. 158 (2018) 376–385.
[53] F. Chekin, V. Myshin, R. Ye, et al., Anal. Bioanal. Chem. 411 (2019) 1509–1516.